Open Loop Performance of a Biomimetic Flapping Foil Autonomous Underwater Vehicle

by

Malima Isabelle Wolf

Submitted to the Department of Mechanical Engineering
in partial fulfillment of the requirements for the degree of

Master of Science in Mechanical Engineering

at the

MASSACHUSETTS INSTITUTE OF TECHNOLOGY

February 2006

Author . . . .
Department of Mechanical Engineering
January 20, 2006

Certified by . . . .
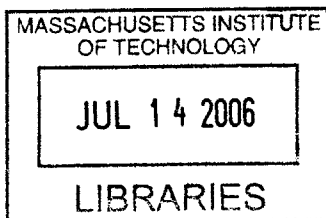Michael S. Triantafyllou
Professor
Thesis Supervisor

Certified by . . . .
Franz S. Hover
Principal Research Engineer
Thesis Supervisor

Accepted by . . . .
Lallit Anand
Chairman, Department Committee on Graduate Students

Open Loop Performance of a Biomimetic Flapping Foil Autonomous Underwater Vehicle

by

Malima Isabelle Wolf

Abstract

Flapping foil propulsion is emerging as an alternative to conventional propulsion for underwater vehicles. MIT's Biomimetic Flapping Foil Autonomous Underwater Vehicle is a prototype vehicle that uses four three-dimensional flapping foil actuators as its means of propulsion. The vehicle providing an opportunity for investigating the efficiency and maneuverability capabilities of a flapping foil system.

This thesis presents and analyzes open-loop performance test data for the Biomimetic Flapping Foil Autonomous Underwater Vehicle. The vehicle is capable of actuating in four different modes of motion, surge, heave, sway, and yaw. These four modes are explored through a range of flapping parameters. For each mode, the parameters were varied to obtain an approximate maximum velocity for the vehicle. Maximum velocity in surge was measured as 1.3827 m/s, in sway as 0.4810 m/s, and in heave as 0.3831 m/s. In yaw, the maximum angular velocity was measured as 80.2 degrees per second.

The performance of the vehicle as reported in this thesis compare well to the previously recorded performance measurements and to theoretical estimates based on the capabilities of the actuators. However, measurements of performance would benefit greatly from better control during testing and from a larger testing space. Developing a more effective means of sway actuation would also benefit the vehicle's performance.

Thesis Supervisor: Michael S. Triantafyllou
Title: Professor

Thesis Supervisor: Franz S. Hover
Title: Principal Research Engineer

Acknowledgments

I would like to thank Professor Triantafyllou and Dr. Franz Hover for all their guidance, and for giving me the opportunity to work on this project.

I would also like to thank Stephen Licht for his help with everything BFFAUV and his guidance in the lab.

I'd like to thank Professor Techet, Victor Polidoro, Karl McLetchie, Keith Lim, Fred Cote, and Mark Belanger for advice and assistance with all the problems encountered over my time in the lab.

I'd like to thank all my coworkers in the Towtank, Vicente, Pradya, Andrew, Lauren, Matt, and Matt, for making this a great lab to work in.

On the personal side, I'd like to thank all my advisees at Fenway House for keeping me grounded. I'd like to thank Rydia and Rachel and all my friends for their support. I'd like to thank my parents, Margo and Stephen, for all their love, encouragement, and support. Lastly, I'd like to thank my sister, Violetta, for supporting me, especially during our time together at MIT. Without her my time here would have been very different.

Contents

List of Figures

9

List of Tables

Chapter 1

Introduction

1.1 Thesis Objective

Many aquatic animals use flapping foils as their primary means of propulsion. While there is a wide variety of aquatic species that employ pectoral swimming, including sea lions, sea turtles, penguins, and pectoral swimming fish, they all use propulsion with similar kinematics and have similar fin geometry. These animals have been found to attain similar speeds [18] [19] and maneuverability [17] to those of tail swimming fish, and are much more agile than any man made underwater vehicle.

M.I.T.'s Biomimetic Flapping Foil Autonomous Underwater Vehicle was built to explore the use of oscillating foils as the primary source of motive power for an autonomous vehicle. By utilizing locomotion similar to that of pectoral swimming marine animals, the vehicle combines the cruising capabilities of vehicles with conventional propulsion systems with improved maneuvering capabilities.

In this thesis, the basic performance of the vehicle is evaluated, both theoretically and experimentally. Cruising performance is explored, as well as maneuvering performance in terms of heave performance, sway performance, and yaw performance. Experimentally, a wide range of flapping parameters is explored for each motion, attempting to find the upper and lower limits to the vehicle's performance.

13

1.2 Previous Work

Research into flapping foil vehicles has been driven by increasing interest in high efficiency and high maneuverability vehicles. Vehicles with conventional propulsion are unsuited for use in confined spaces or difficult flow conditions, near underwater structures or in current and waves. Flapping foil vehicles have the potential to be used in such situations.

Previous work in flapping foil research has included research into both the performance of flapping foil vehicles and the performance of the actuated foils themselves.

Many of the flapping foil vehicles previously built have taken the form of tail swimming animals. RoboTuna, a vehicle designed to mimic the motion of a tuna, was designed and constructed by Dave Barrett at M.I.T. in 1994 [2]. RoboTuna II, the next generation robotic tuna, was built by Dave Beal, Mike Sachinis, and Mike Jakuba in 2000 [3] [5]. These robots mimic the tail swimming of a tuna by actuating six degrees of freedom in the body and tail. Both versions of the RoboTuna were carriage mounted, making force and velocity measurements more reliable, as well as allowing external power for a more compact vehicle.

Several free swimming vehicles with similar kinematics have been built. The RoboPike, designed and fabricated by John Kumph at MIT in 1996 [9], mimics a tail swimming pike using two degrees of freedom to control body curvature and one degree of freedom to control the angle of the caudal fin. The vehicle, which measures in with a length of about 0.81 meters and displacement of 3.6 kilograms, can achieve a top speed of approximately 0.2 body lengths per second. The Vorticity Control Unmanned Underwater Vehicle (VCUUV) was developed by Jamie Anderson and her colleagues at Draper Laboratory [1] in 1997. Similar in locomotion to a tuna, the VCUUV has a four degree of freedom tail section. The vehicle is 2.4 meters in length and displaces 136 kilograms with a top speed of 0.5 body lengths per second. Both of these vehicles use their tails for propulsion with steering assistance from pectoral fins. Tail swimming vehicles that mimic the motion of dolphins have also been built. Motomu Nakashima and his colleagues at Tokyo Institute of Technology
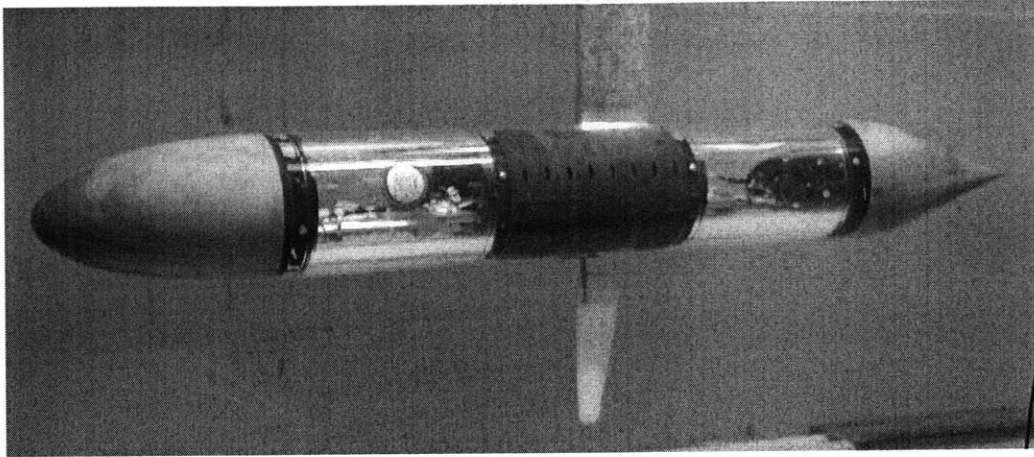
Figure 1-1: SeaLion, a pectoral swimming vehicle.

built two robotic dolphins, the first generation vehicle pneumatically powered, the second using a battery system. Both dolphins used two degree of freedom tails for propulsion. Similar systems were mounted to carriage systems for more detailed analysis [15].

Other swimming vehicles are beginning to take the form of pectoral swimming animals, similar to the vehicle explored in this thesis. The SeaLion is a carriage mounted pectoral swimming vehicle designed and built by Craig Martin in 2001, shown in Figure 1-1 [13]. The SeaLion's single foil is actuated in roll and twist.

Naomi Kato has lead a program of research developing pectoral swimming robotics and exploring their performance. Birdfin, a carriage-mounted vehicle with a three degree of freedom fin, was used by Kato and Liu to explore the performance of lift-based and drag-based pectoral propulsion in uniform flow and in still water [6]. Kato and his colleagues built two generations of robotic fish with two pectoral fins, similar to bass fish [8], shown in Figure 1-2. The fish performs a drag based form of propulsion, similar to rowing, with its two degree of freedom fins. The later PLATYPUS robot used two pairs of three degree of freedom fins for propulsion. The vehicle is 1.36 meters in length with fins that have a chord length of 0.1 meter and a span of 0.8 meters. The vehicle's performance has been explored by performing docking maneuvers in the presence of currents and wall following maneuvers around a 1.5 meter diameter
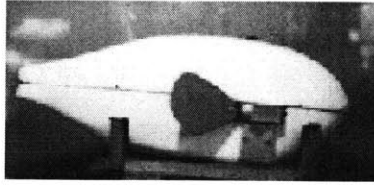
Figure 1-2: Robotic fish designed by N. Kato.

Figure 1-3: Nekton Research LLC's flapping foil vehicle. [16]

cylinder [7].

Researchers at Nekton Research LLC have designed a vehicle with two pairs of pectoral fins, used for both lift based and drag based motion, recently discussed in *Science* [16]. Each flipper can be controlled independently, allowing for a wide range of movement. This vehicle, nicknamed "Madeline" is shown in Figure 1-3.

1.3   Coordinate Conventions and Kinematics

Describing the motion of the vehicle is an important step for evaluating its performance. In this thesis, the motion of the vehicle is described in similar terms to the motion of a ship. First we define a right handed coordinate system corresponding with the vehicle body with axes X_1, X_2, and X_3. The center of the coordinate system is at the geometric center of the vehicle. The X_1 axis points toward the bow of the

16
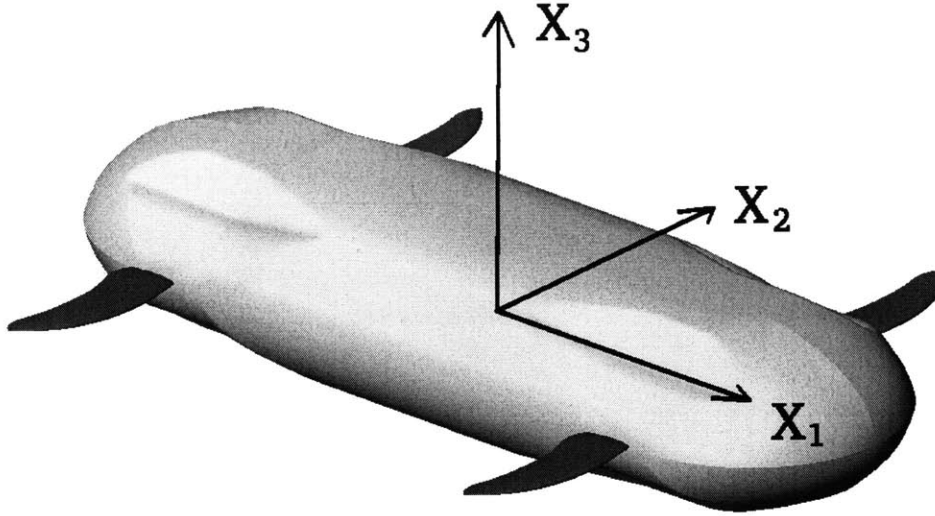
Figure 1-4: Vehicle coordinate system.

vehicle, the X_2 axis points to the port side, and the X_3 axis points up. Figure 1-4 shows the vehicle and its coordinate system. The bow of the vehicle is pointed to the right in this figure.

Six degrees of freedom in the vehicle's motion are considered, x_1, x_2, x_3, x_4, x_5, and x_6. The first three coordinates correspond with the linear degrees of freedom. The x_1 direction corresponds with surge along the X_1 axis. x_2 corresponds with sway along the X_2 axis. x_3 corresponds with heave along the X_3 axis. The second three coordinates correspond to the rotational degrees of freedom. x_4 corresponds with roll, rotation about the X_1 axis. x_5 corresponds with pitch, rotation about the X_2 axis. x_6 corresponds with yaw, or rotation about the X_3 axis.

The motion of the vehicle's flapping foils is also a major concern. Each foil's position is described with three parameters with respect to the vehicle, roll angle, twist angle, and direction. Roll angle, ϕ, corresponds with rotation of the foil about its base in the X_1 direction. Twist angle, θ, corresponds with rotation of the foil about its base in the X_2 direction. We consider the positive direction of both of these angles to be rotating up, toward the positive X_3, for all foils. Figure 1-5 shows the foil coordinate conventions for the front starboard foil. Direction refers to the initial

17
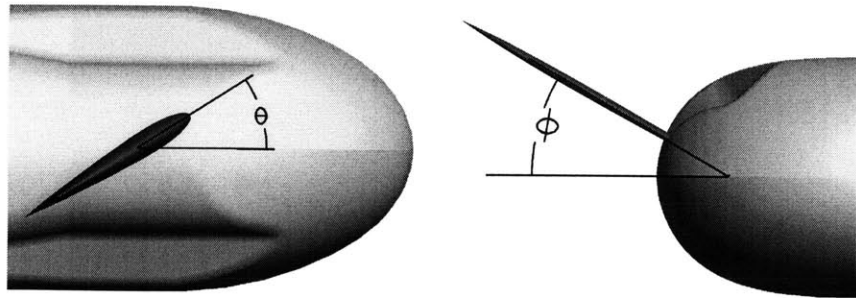
(a) Twist angle.

(b) Roll angle.

Figure 1-5: Angular coordinates of front starboard foil.
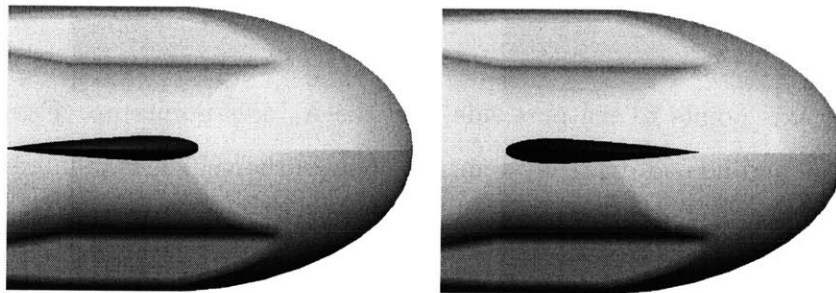
(a) Normal direction.

(b) Reverse direction.

Figure 1-6: Direction for front starboard foil.

position of the foil motion. Normal direction corresponds to the foil zero position with the foil being held in the X_1-X_2 plane with the leading edge pointing toward the front of the vehicle. Reverse direction corresponds to a similar position with the leading edge of the foil pointed toward the rear of the vehicle. Switching from normal to reverse direction switches the handed-ness of the angular coordinates. Figure 1-6 shows the front starboard foil oriented in normal direction (Figure 1-6(a)) and reverse direction (Figure 1-6(b)). In these figures, the vehicle faces to the right, with each picture showing the bow of the vehicle.

The kinematics of the foils can be described in terms of these parameters. The

18

foil rolls about its origin with angular position $\phi(t)$ and twists about its origin with angular position $\theta(t)$. Both follow a sinusoidal motion with the same frequency. The equations of motion for $\phi(t)$ and $\theta(t)$ are

$$\phi(t) = \phi_0 \sin(\omega t) + \phi_{bias} \tag{1.1}$$

$$\theta(t) = \theta_0 \sin(\omega t + \psi) + \theta_{bias} \tag{1.2}$$

where ϕ_0 and θ_0 are the roll and twist amplitudes, respectively, ω is the flapping frequency, ψ is the phase angle between the two motions, and ϕ_{bias} and θ_{bias} are bias angles from zero.

A phase angle of $\pi/2$ is always used so the equations above simplify to

$$\phi(t) = \phi_0 \sin(\omega t) + \phi_{bias} \tag{1.3}$$

$$\theta(t) = \theta_0 \cos(\omega t) + \theta_{bias} \tag{1.4}$$

Chapter 2

Experimental Apparatus and Methods

The experiments presented in this thesis were conducted in the M.I.T. Alumni Pool using the Biomimetic Flapping Foil Autonomous Underwater Vehicle. The basic design of the BFFAUV was described by Licht et. al. [10] In the context of this thesis, the actuators and foils used to drive the vehicle are of particular interest, as are the sensors used to record performance data. Overall vehicle form and mass are also important and are discussed in greater detail in Section 3.1.

2.1 The Biomimetic Flapping Foil Autonomous Underwater Vehicle

The Biomimetic Flapping Foil Autonomous Underwater Vehicle was designed as a test platform for the use of flapping foils as the sole propulsion source for an underwater vehicle. As a proof-of-concept vehicle for flapping foil propulsion, the design of the vehicle focuses on accommodating the actuators and their support and control systems.

The vehicle's design is symmetric. The actuators are each placed so that the center of rotation for their foils is from 0.602m the X_1 axis and 0.21m from the X_2 axis.

21
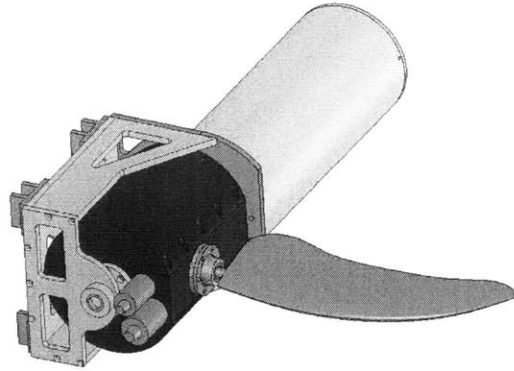
Figure 2-1: A BFFAUV actuator and foil.

The fairing is also symmetric, measuring 1.98m in length, 0.66m across, and 0.406m in height, displacing 0.372 cubic meters, or approximately 372 kg. The symmetric design allows the vehicle to move as easily in reversed directions and places the centers of mass, gravity, and drag near the geometric center of the vehicle.

2.1.1 Actuators

The BFFAUV's actuators are designed as stand-alone, water-proof units. The actuator, shown in Fig. 2-1, is divided into two sections, each with its own housing. An aluminum frame supports the two cylindrical housings. The longer cylinder is fixed to the frame, while the shorter cylinder rolls about its axis with respect to the longer cylinder. The actuator uses a 190- and 15-W direct current brush motor with optical encoders (Litton-Polyscientific, Blacksburg, VA) to actuate in roll and pitch, respectively. The actuators have a 160° range of motion in roll and unrestricted motion in pitch. Each actuator has an on-board motor control circuit, including an Ethernet-enabled two-axis motion control card. Ethernet and power cables connect each actuator to the central hub and power system.
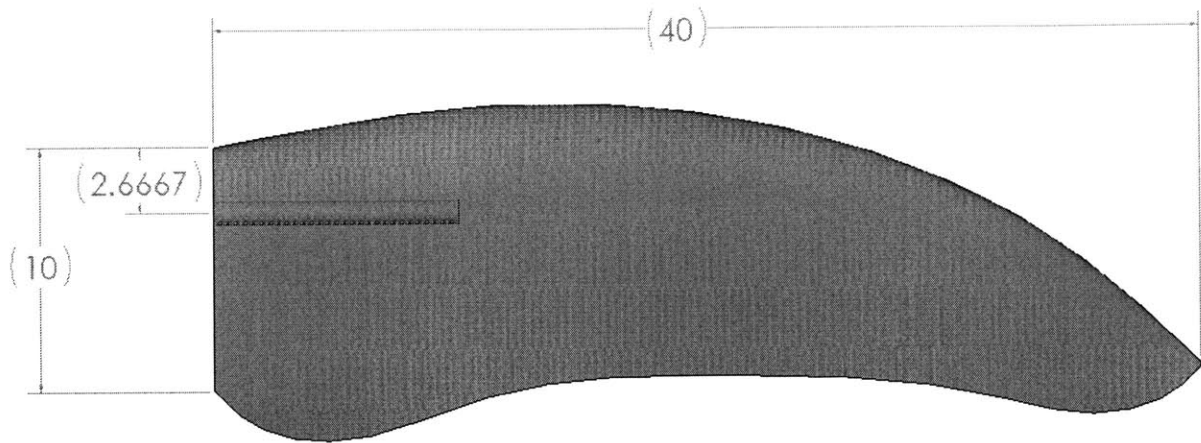
Figure 2-2: The foil used on the BFFAUV.

2.1.2   Foil Description

The vehicle's foil, shown in Fig. 2-2, is designed to resemble the pectoral fin of a sea turtle. The fin measures 40 cm in length and has an average chord of 10.1 cm, giving a foil ratio of approximately 4:1. The projected area of the foil is approximately 393 square centimeters. The foil's cross sections are airfoils taken from the NACA-00 series. At its largest chords, the foil has a NACA-0012 profile, tapering down to a NACA-0020 at its tip. The foil tapers profiles for ease of construction. A welded titanium frame and shaft support for the Shore A 70 hardness polyurethane rubber that is the bulk of the fin. The fin has some flexibility, especially at the trailing edge, due to its construction.

2.1.3   Fairing

The vehicle's fairing serves several purposes. In addition to protecting the vehicle's components, the fairing provides a hydrodynamic shape for the vehicle. The vehicle's outer dimensions and displacement are shaped by the fairing. As given in Section 2.1, the vehicle measures 1.98m in length, 0.66m across, and 0.406m in height and displaces 0.372 cubic meters. The fairing forms a central section that is approximately cylindrical. The flattened cross-section is 0.406m in height and 0.66m in width and has
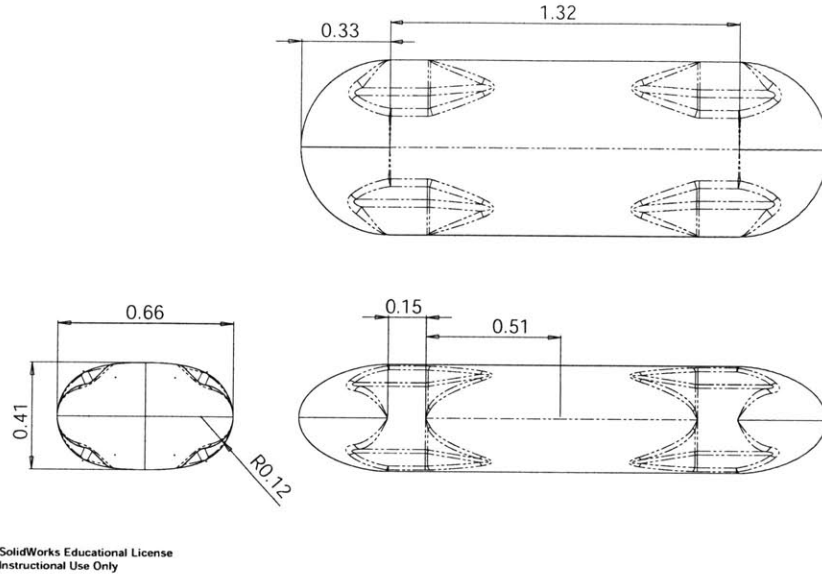
Figure 2-3: The basic shape of the fairing.

an area of 0.2245 square meters. The flattened cylindrical section is 1.32m in length, and is capped on each end with a dome 0.33m in height. The otherwise smooth form has small indents surrounding each actuator, creating a cylindrical section with radius 0.12m. These indents allow the fins to rotate through their full range of motion. The outer form of the fairing is shown in Fig. 2-3.

The fairing is assembled onto the vehicle as two halves. The fairing is split along the vehicle's horizontal center plane. The assembled fairing covers the vehicle entirely except for a few cut-outs. By each actuator is a vertical slot approximately 2.5 cm wide that surrounds the shaft of each actuator's fin. The slots are long enough to allow the actuator to move the fin through its full range of roll and pitch motion. A cut-out on the top of the vehicle gives access to the main power switches and to the lifting blocks. There are several cut-outs on the fairing that allow a clear The Doppler Velocity Log (see Section 2.1.4) and its protective rods stick out of a large cut-out on the underside of the vehicle, while four circular holes approximately 4.7 cm in diameter are used as clearance for the altimeter beams. In addition to the

24
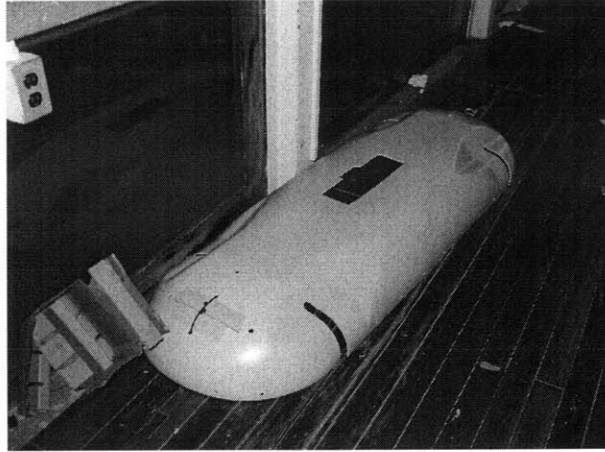
Figure 2-4: The upper half of the fairing.

open cut-outs on the fairing, there are a pair of hatches located at the fore and aft of the vehicle, used to secure weights and floats used as trim adjustments inside of the vehicle. Fig. 2-4 shows the upper half of the fairing. In some configurations, two additional fins are attached to the vehicle to act as stabilizers. The fins are located on the vertical centerline of the vehicle, located approximately 0.65 meters from the center of the vehicle, as show in Figure 2-5. These fins are very similar to the foils used for vehicle propulsion. They are mounted to the fairing by brackets directly bolted to the fin frame.

The shells are created from thermoformed polyethylene. Polyethylene is a common material for thermoforming which is also easily machinable and can be welded together. Polyethylene has a density similar to that of water and is chemically resistant to a wide variety of solvents. Polyethylene also comes in a wide variety of standard colors, allowing us to chose a bright yellow color for easy visibility underwater. All of these factors combine to make polyethylene an ideal material for our fairing.

The basic fairing was manufactured by Trans Form Plastics of Danvers, MA, using a mold made by Beverly Pattern of Beverly, MA. The mold consists of a male core assembled from machined polyurethane boards. The mold is the shape of one half of the fairing, cut along the horizontal plane. The core is continues down vertically for

25
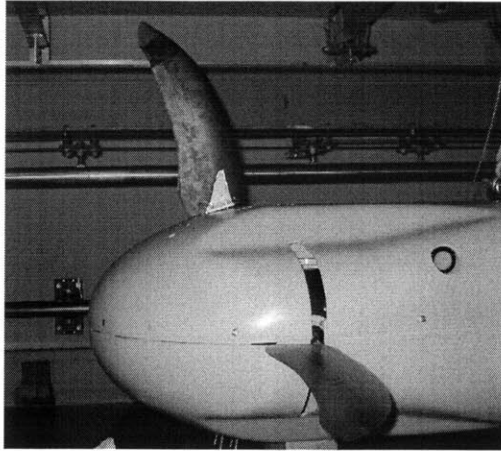
Figure 2-5: The upper stabilizing fin mounted on the rear of the vehicle.

about 5 cm to the mold's wooden vacuum box support. Each board is approximately 10.2 cm in thickness, resulting in a mold made out of three layers.

The fairing is made of two halves, thermoformed and adjusted by Trans Form Plastics. First, mold pieces were thermoformed from 1/4" thick polyethylene blanks. The shells were trimmed from the blanks using a wooden trimming jig made at Trans Form. The upper and lower halves of the fairing were manufactured identically up to this point. Next, the upper half was finished by drilling holes along the edge of the fairing to be used as clearance holes for fasteners. The lower half includes an additional layer of plastic welded onto the inside of the fairing. This layer forms a 10 cm wide rim backing the meeting of the two halves of the fairing. The two halves butt together along the mid-line of the vehicle, and the rim overlaps them both. The fastener receptacles are mounted on the back of this strip, lining up with the holes in the upper half of the fairing.

About thirty fasteners were used to secure the two halves of the fairing together. The fasteners used were Dzus standard line quarter-turn fasteners by Southco. Fig. 2-6(a) shows a diagram of a fastener and its receptacle in use. The fastener itself is shown in Fig. 2-6(b) and a mounted receptacle is shown in Fig. 2-6(c). The fastener is inserted through clearance holes in the materials being fastened. A slit in the end of the fastener slips over the wire receptacle, and the fastener is then turned a
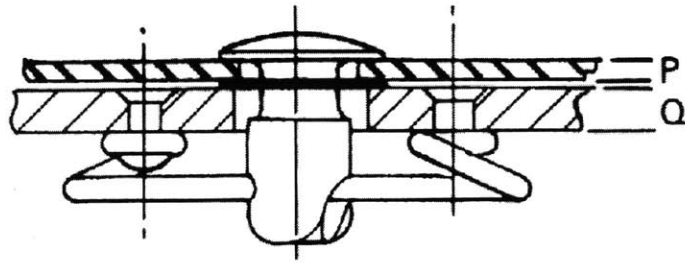
(a) Mounted Dzus fastener.
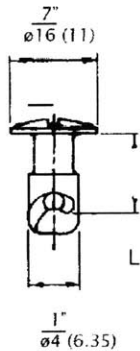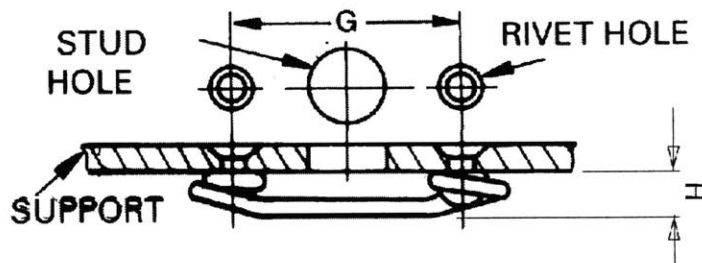
(b) Fastener.   (c) Receptacle.

Figure 2-6: Size 4 Dzus fastener and hole pattern. (©Southco.)

quarter of a turn, locking the fastener over the receptacle, as shown in Fig. 2-6(a). The BFFAUV uses size 4 fasteners, which are 1/4" in diameter. The corresponding S-spring receptacles are mounted to the inside of the fairing rim with 3/32" rivets. When the fairing is fastened shut, it is tight enough around the vehicle that no direct attachment is required. The hatches on the upper half of the fairing are also secured using Dzus fasteners.

2.1.4 Sensors

The BFFAUV employs a wide selection of sensors, used both for closed loop control of the vehicle and for recording the performance of the vehicle. At the center of the vehicle is a Crossbow six-axis accelerometer.

The vehicle uses three Tritech PA500 altimeters. One altimeter is mounted in

27

the nose of the vehicle and is used for range finding during control and performance testing. The other two altimeters are mounted on the starboard side of the vehicle, one just behind the forward fin, and one just in front of the rear fin. The pair can be used to judge distance to an object on the starboard side, and in the case of a wall, the pair can be used to determine the vehicle's yaw angle with respect to the wall. The altimeters have a six degree conical beam with an operating range of 0.3 to 50 meters. The altimeters are 18 cm in length, 4.7 cm in diameter, and weigh 1.1 kg each.

The vehicle also uses a 1200 kHz Workhorse Navigator Doppler Velocity Log (DVL) from RD Instruments. The DVL is installed directly under accelerometer, beneath the center of mass of the vehicle. The DVL has a wide range of capabilities, including measuring surge, heave, and sway velocities, heave altitude, roll and pitch angles, and heading. The DVL uses a four beam Janus array, with convex transducers with a thirty degree beam angle. The operating range of the DVL is 0.5 to 30 meters and can detect velocities up to 10 m/s.

Chapter 3

Evaluation of Theoretical Vehicle Performance

In this section, a theoretical evaluation of the performance of the Biomimetic Flapping Foil Autonomous Underwater Vehicle is presented. This theoretical evaluation serves as a basis of comparison for the experimental results discussed in Chapter 4.

3.1 Vehicle Body Parameters

The physical properties of the vehicle directly affect its performance. The maximum velocities and accelerations achieved will reflect the mass and moments of inertia of the vehicle, the hydrodynamic drag on the vehicle, and the added mass of the vehicle while accelerating.

3.1.1 Mass and Moments of Inertia

The mass and moments of inertia of the vehicle were estimated rather than measured directly. The mass of the vehicle was estimated by determining the volume held inside the fairing, including the fairing itself. Assuming that the vehicle is neutrally buoyant, the vehicle's mass is should be the same as mass displaced by the fairing. By using this technique, the mass of the vehicle was estimated to be 372 kg.

Table 3.1: Vehicle Moments of Inertia, in $kg \cdot m^2$

$I_{1,1}$	$I_{2,2}$	$I_{3,3}$
10.3	72.6	75.5

Moments of inertia were estimated from a computer model of the vehicle. The model places components in their relative positions and and assigns them each a uniform density which will give the component its known mass. Water inside of the vehicle's hull was approximated by placing volumes of water inside the model which were shaped to conform around other components. The modeling software generates the moments of inertia based on the components. Table 3.1 gives these moments of inertia.

3.1.2 Drag Coefficients

An estimate of the vehicle's hydrodynamic drag coefficient would best be found through comprehensive testing. Rough estimates of the vehicle's hydrodynamic drag can be found based on shape parameters.

Looking at surge motion, it is simplest to approximate the vehicle as an ellipsoid. Assuming a vehicle speed of approximately 1 m/s, the vehicle is typically operating at a Reynolds number of approximately 10^6. With a vehicle length of 1.98 m, a width of 0.66 m, and a height of 0.41 m, the vehicle's form factor is approximately 3.7:1. Based on Figure 19 from Chapter 3 of Hoerner [4], if the vehicle is approximated by a perfect ellipsoid, it's coefficient of drag could be as low as 0.08. This drag coefficient is strongly affected by imperfections in the fairing. Holes, projections, and roughness all effect the coefficient of drag. Based of Figure 21 from the same section of Hoerner, a blunt cylinder of the same form factor would have a coefficient of drag of approximately 0.85. The vehicle's coefficient of drag should be assumed to be somewhere between these two estimates.

In the case of heave and sway motion, drag parameters can be similarly constructed. In both cases, the drag of the vehicle can be modeled approximately as the

two-dimensional drag of a cylinder, representing the untapered portion of the fairing body, combined with the three dimensional drag of a sphere, representing the nose and tail cone of the fairing. In the case of sway, the vehicle is operating under a Reynolds number of approximately $2 \cdot 10^5$, and in the case of heave, the Reynolds number is approximately $3 \cdot 10^5$. Assuming turbulent conditions, the coefficient of drag for the spherical portion would be approximately 0.1, and for the cylinder the coefficient of drag would be approximately 0.3, yielding a drag coefficient of approximately 0.27 based on frontal area.

An estimate of the vehicle's drag in yaw can be found using slender body theory. By integrating along the X_1 axis and approximating the vehicle body as an ellipsoid, the rotational drag factor on the vehicle can be approximated by

$$C_D \cdot A = \int_L \pi x^2 a^2(x) \tag{3.1}$$

where x is position along the X_1 axis and $a(x)$ is the height of the vehicle at that position. Calculating the value numerically, we find $C_D \cdot A = 0.0614$.

3.1.3 Added Mass

Added mass calculations are necessary for the vehicle in the $x_1 x_1$ direction and in the $x_6 x_6$. While extensive testing would be the best way to determine these coefficients, approximate solutions can be found using theoretical means. For the $x_1 x_1$ added mass, the equation for the added mass of an ovoid can be used. The added mass equation for our vehicle is then

$$m_{x_1 x_1} = \rho \frac{2}{3} \forall \tag{3.2}$$

where ρ is the fluid density and $\forall$ is the volume of the body. In our case, the body density is equal to that of water, so we can substitute in M, the vehicle mass, for $\rho \forall$, yielding

$$m_{x_1 x_1} = \frac{2}{3} M = \frac{2}{3} 372 = 248 kg \tag{3.3}$$

To estimate the added mass in the $x_6 x_6$ direction, slender body theory can be

used. Slender body theory gives the added mass of the vehicle in the $x_6 x_6$ direction as

$$m_{x_6 x_6} = \int_L x^2 M_1 1(x) dx \qquad (3.4)$$

where $M_1 1$ is the added mass of the cross section at x. If it is assumed that the vehicle has an ellipsoidal cross section $a(x)$, the equation becomes

$$m_{x_6 x_6} = \int_L \rho \pi x^2 a^2(x) dx \qquad (3.5)$$

Computing this calculation for the vehicle, an added mass of $m_{x_6 x_6} = 61.4$ kilograms is found.

3.2 Performance Estimates

3.2.1 Surge Performance

The performance of the actuators in surge motion has been estimated in a few ways. Actuator performance can be calculated based on the potential power output of the motors. Licht et. al [10] presented such an estimate based on known torque-shaft speed curves and power and roll acceleration curves. Experimental measurements of the thrust output of the actuators taken by Lim [11] and McLetchie [14] provide another way to estimate the thrust output of each actuator.

Licht [10] estimates the performance of the vehicle based on the limits of the roll motors. Two factors limit the performance of the motors. The first limit considered is the roll motors' power output. The power output is at its maximum at the moment of maximum foil angular rotation, as the foil pulls through the middle of its stroke, when $\phi(t) - \phi_{bias} = 0$. The second limit is the ability of the motors to supply the zero-speed torque required at the moment of maximum foil angular acceleration. In both cases, the power or torque required of the motors is dependent on two factors, the speed of the vehicle through the water and the coefficient of thrust, C_T, that the actuator must achieve to counter the drag of the vehicle body. For a given C_T, a

curve of how the required power or torque varies with velocity can be drawn. The maximum velocity for a given C_T occurs when the power-velocity or torque-velocity curve reaches the maximum output of the motors.

A variety of coefficients of thrust were considered in [10]. A well-streamlined vehicle might have a low required coefficient of thrust, approximately 0.1. With this low a coefficient of thrust, the vehicle should be able to achieve a maximum velocity of over 2.0 meters per second. A higher required coefficient of thrust, 0.66, which is easily obtainable for the BFFAUV, the maximum velocity would be approximately 1.5 meters per second. By the estimates of the paper, the vehicle should have a maximum velocity in the range of 1.5 to 2 meters per second.

Lim [11] and McLetchie [14] provide another avenue for estimating the performance of the BFFAUV. Both did controlled studies of the performance of the BFFAUV actuators. By comparing their actuator motion and configuration parameters to those used currently on the vehicle, it is possible to estimate the thrust output of the actuators.

In order to compare the current actuator configuration to the previous work, the same non-dimensional parameters are used as in these previous works. The dimensionless parameters defining each motion are maximum angle of attack, α_{max}, heave amplitude, $h_{0.7/c}$, and Strouhal number, St. All of these parameters are defined at a radius that is 70% of the foil span.

Angle of attack, $\alpha(t)$, is defined as

$$\alpha(t) = \arctan(\frac{r\phi_0\omega\cos(\omega t)}{U}) - \theta_0\cos(\omega t) \tag{3.6}$$

where r is radius, ϕ_0 is twist magnitude, ω is flapping frequency, and θ_0 is roll magnitude. Maximum angle of attack is defined as the maximum angle of attack at $R_{0.7}$, the radius 70% along the span of the foil, over a single period, given as

$$\alpha_{max} = \max\{\alpha(t)\} \tag{3.7}$$

The non-dimensional swept arclength, known as the heave amplitude, is defined

33

as

$$h_{0.7}/c = R_{0.7}\phi_0/c \tag{3.8}$$

where c is the average chord of the foil.

The Strouhal number is defined as

$$St = \frac{2h_{0.7}f}{U} \tag{3.9}$$

where f is the flapping frequency and U is the flow speed past the foil, effectively the opposite of the vehicle's velocity.

By evaluating the motion of the BFFAUV in terms of these parameters, an estimate of the coefficient of thrust can be found for our foil configuration. Several different parameters are necessary to calculate the dimensionless parameters. Some of the parameters are unchanging physical properties of the foil and actuator, and some are defined by the chosen kinematics. The one property that varies unpredictably is U, the flow velocity. Rather than generating one coefficient of thrust from a given set of foil kinematics, a curve of coefficient of thrust in terms of velocity will be generated.

The highest value of $h_{0.7}/c$ explored by Lim and McLetchie was $h_{0.7}/c{=}2.0$, which limits the range of foil motion that can be compared to prior results. The lowest roll amplitude investigated in surge experiments was 30 degrees, yielding a heave to chord ratio of $h_{0.7}/c = 2.1254$, thus comparisons can only be drawn for the lower range of surge motion explored. Figure 3-1 shows the predictions of C_T based on that data. This calculation is expected to overestimate the value of C_T for the given foil motion parameters due to the difference in $h_{0.7}/c$. Higher values of $h_{0.7}/c$ correspond to lower values for the coefficient of thrust.

While a prediction of the maximum speed of the vehicle cannot be made based on these data, they can be used to provide a rough estimate of maximum velocity for surge motion with a flapping frequency of 1 Hz, $\phi_0 = 30$, and $\theta_0 = 40$. Using a similar method for balancing coefficient of thrust and coefficient of drag as presented

34
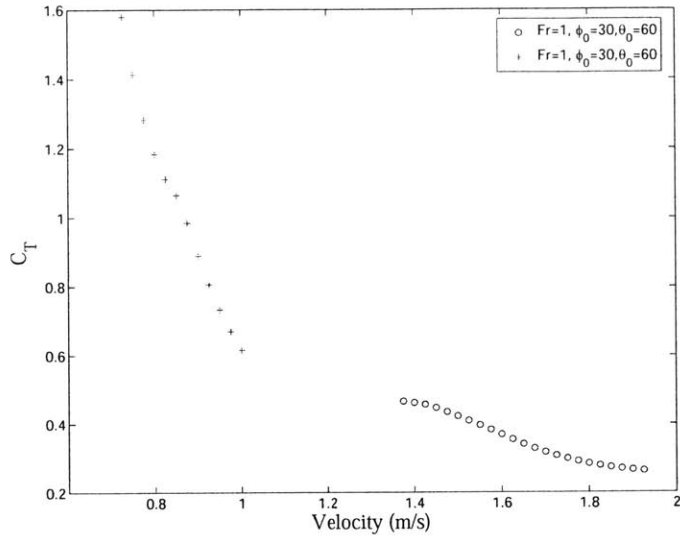
Figure 3-1: Estimate of C_T based on experimental results from Lim [11].

by Licht [10], we use the relationship

$$C_T = C_D \frac{A_{vehicle}}{A_{foils}} \tag{3.10}$$

to estimate C_T, where $A_{vehicle}$ is the frontal area of the vehicle and A_{foils} is the total area of the foils. Substituting in with an estimated coefficient of thrust of 0.3, we find

$$C_T = 0.3 \cdot \frac{0.22443}{4 \cdot 0.4 \cdot 0.10125} = 0.4156 \tag{3.11}$$

Based on projections from the coefficient of thrust series for surge with flapping frequency of 1 Hz, roll amplitude of 30 degrees, and twist amplitude of 40 degrees, the vehicle should be able to attain a top speed with this motion of approximately 1.1 meters per second.

3.2.2 Yaw Performance

The BFFAUV's yaw performance can be estimated using Morrison's equation. Morrison's equation for yaw states that

$$M_{foils} = \Omega^2 m_{x_6 x_6} + \Omega^2 \frac{1}{2} \rho C_D \cdot A \qquad (3.12)$$

where M_{foils} is the moment generated by the foils, Ω is the angular velocity of the vehicle, ρ is the density of water, and $m_{x_6 x_6}$ and $C_D \cdot A$ are the added mass and drag factor as found previously.

The moment generated by the foils can be estimated by a method similar to that used by Licht [10] to estimate the surge performance of the foils. The moment generated by the foils is equal to the thrust force generated by the foils multiplied by the radius of action from the vehicle body that the foils are acting at. The perpendicular component of the lever arm, in the X_2 direction, is defined as the distance from the vehicle's centerline to the foil's center of rotation plus the distance from the foil's center of rotation to 70% along its span. The distance from the vehicle's centerline to the foil's center of rotation is 0.20 meters, and the distance from the center of rotation to 70% of the foil's span is 0.49 meters, giving a combined radius of action of 0.69 meters. With this expression for the moment from the foils, the force balance equation becomes

$$0.69 \frac{1}{2} \rho U^2 A_{foils} C_T = \Omega^2 m_{x_6 x_6} + \Omega^2 \frac{1}{2} \rho C_D \cdot A \qquad (3.13)$$

where U is the velocity of the fin through the water. The distance from the center of the vehicle to 70% of the span is 0.85 meters, so $U = 0.85\Omega$. Based on this relationship, the coefficient of thrust achievable by the foils limits the maximum yaw angular velocity. The maximum velocity will be where

$$C_T = \frac{61.4 + \frac{1}{2} \rho 0.0614}{0.69 \frac{1}{2} \rho A_{foils} .85^2} = \frac{92.1}{39.9} = 2.3 \qquad (3.14)$$

From Licht's performance estimates for the motors [10], we can estimate the maximum

fin velocity which corresponds to $C_T = 2.3$. Maximum roll motor power output is the motor parameter that is most limiting in this case. With $C_T = 2.3$, the maximum velocity predicted by the limit of the roll motor power is approximately 1.1 meter per second at the fin. With the distance from the center of the vehicle to 70% of the fin span as 0.85 meters, this gives a maximum rotational velocity of 1.3 radians per second, or 75 degrees per second.

3.2.3 Sway and Heave Performance

Sway and heave motion are very similar modes of motion, and thus require a similar analysis. As in the estimate of surge performance, the equation

$$C_T = C_D \frac{A_{vehicle}}{A_{foils}} \tag{3.15}$$

will be used to estimate the coefficient of thrust required to propel the vehicle at different speeds. From Section 3.1.2, the ideal coefficient of drag for the vehicle in sway and heave is about 0.27. The coefficient of drag may be higher because of imperfections in the fairing, such as projections and roughness. In the case of sway, the frontal area of the vehicle is 0.6807 square meters, and in the case of heave, it's 1.0210 square meters. The total area of all four foils is 0.162 square meters.

Estimating the coefficient of thrust in the cases of sway and heave is difficult because the foils are actuated in drag-based forms of motion as opposed to the lift-based form used in surge and yaw motion. The drag-based form of motion is similar to rowing, however, the yaw and twist angle transition sinusoidally, rather than execute a distinct power-stroke and return-stroke. The motion is detailed in Section 4.1. With the atypical kinematics used, theoretically determining the coefficient of thrust is difficult. Extensive testing would be the best way to determine the thrust coefficient.

Chapter 4

Experimental Performance

A series of experiments were performed to evaluate the Biomimetic Flapping Foil Autonomous Underwater Vehicle's performance.

4.1 Description of Kinematics

Testing each degree of freedom requires a different set of kinematics. For heave, all foils are driven with a 45 degree twist bias angle when ascending or a −45 degree twist bias for descent, and the twist amplitude is set to 45 degreed. This creates a drag based form of propulsion where in one direction, the fin pulls through the water feathered for reduced drag in one half of the stroke and then pushes with the flat of the fin on the other half creating thrust. There is some horizontal component to the thrust, which is balanced by reversing the direction of the forward pair of fins on the vehicle. The equations of motion for an individual fin while ascending are

$$\phi(t) = \phi_0 \sin(\omega t) \tag{4.1}$$

$$\theta(t) = \pi/4 * \cos(\omega t) + \pi/4 \tag{4.2}$$

Figure 4-1 shows the angular position of a fin during ascent. Each fin follows these equations, but the forward fins are driven in the reverse direction. The motion of each fin creates some thrust aligned with the vehicle's X_1 axis, and to avoid surge
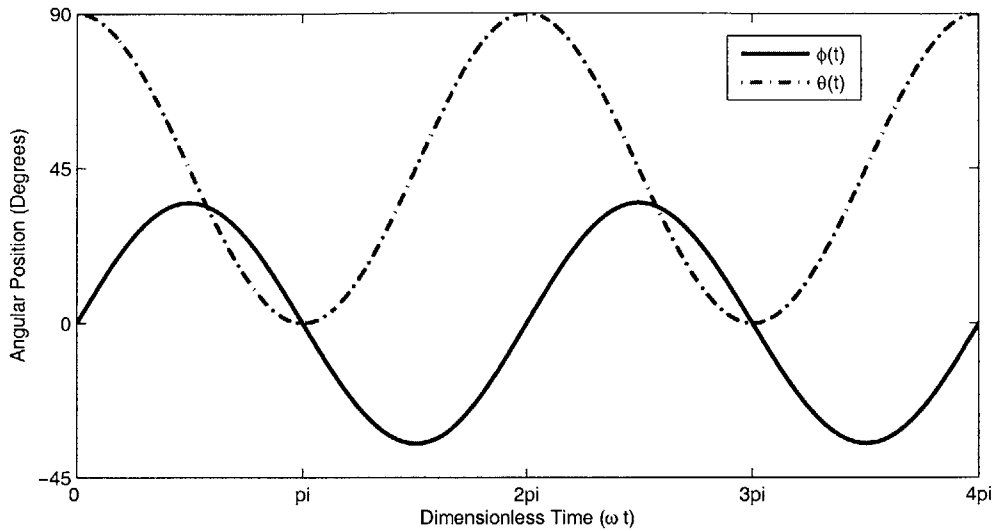
39

Figure 4-1: Fin motion during ascent.

motion, the forward fins are reversed.

During yaw motions, the foils are driven with no twist or roll bias. The equations of motion for an individual fin are

$$\phi(t) = \phi_0 \sin(\omega t) \tag{4.3}$$

$$\theta(t) = \theta_0 \cos(\omega t) \tag{4.4}$$

Figure 4-3 The fins are put into pairs based on which side of the vehicle they are on, port or starboard. One pair of fins is driven in normally, and the other pair of fins is driven in the reverse direction, causing the vehicle to turn.

Individual fin motion in sway mode is similar to the individual fin motion during heave. A positive or negative 45 degree twist bias is used in sway as in heave, creating a similar drag based form of propulsion. In sway, the fins are given a roll bias, creating a horizontal component to the force. Ideally, the roll bias for the fins would be 90 degrees, eliminating the vertical component of the force, but the physical limitations of the vehicle limit the bias to less than 70 degrees. Due to the vertical component of the force, there is some out of plane travel of the vehicle. The following equations
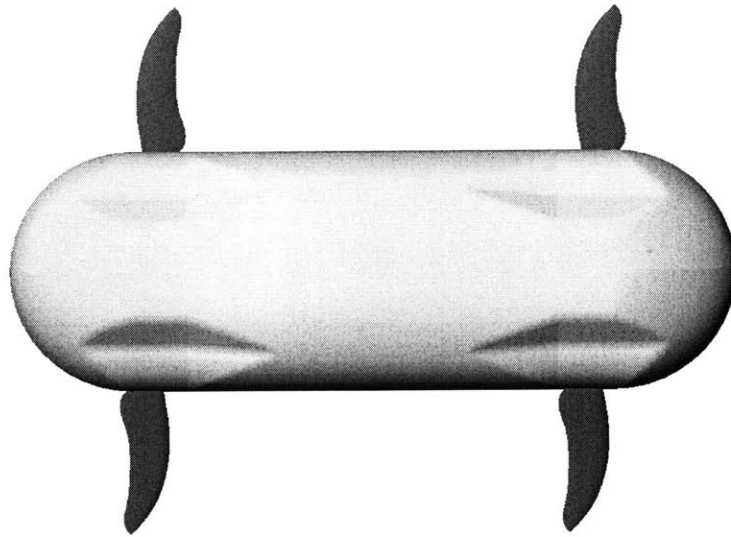
40

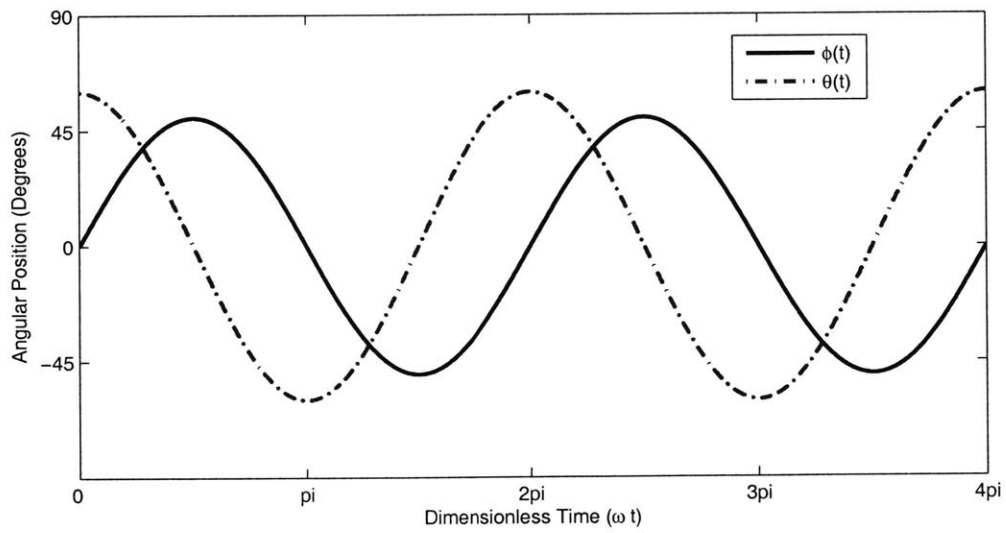Figure 4-2: Fin alignment during counter-clockwise yaw testing.

Figure 4-3: Fin motion during yaw testing.
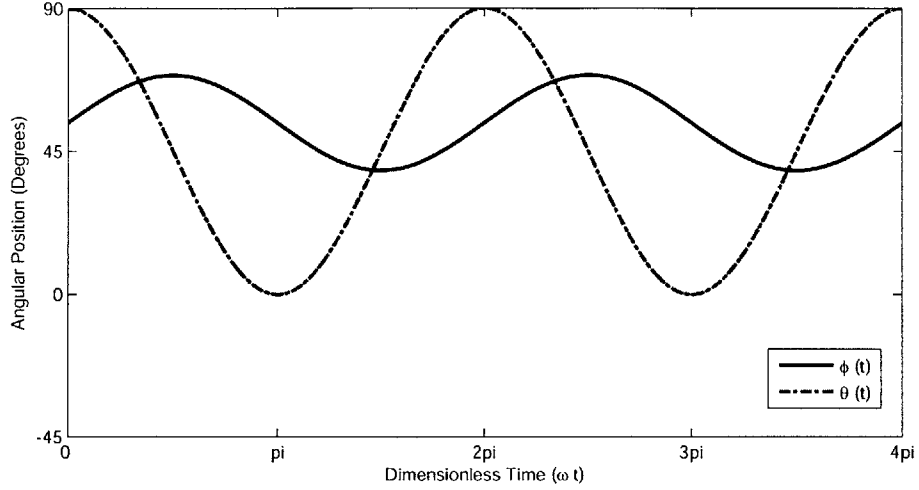
Figure 4-4: Fin motion during sway testing.

express the basic motion of a fin during sway swimming, Figure 4-4 shows the angular position.

$$\phi(t) = \phi_0 \sin(\omega t) + \phi_{bias} \qquad (4.5)$$

$$\theta(t) = \pi/4 * \cos(\omega t) + \pi/4 \qquad (4.6)$$

The forces generated by the fins during sway motion create roll moments about the vehicle. These forces need to be matched to reduce their effect on the vehicle. The roll moment created by a fin with positive roll bias is countered by the roll moment created by a fin with negative roll bias. Thus, to balance the moments created by the fins, two fins need to be "up" and two fins need to be "down". In our experiments, the fins are paired into starboard and port fins. One pair of fins is biased positively in roll, and the other will be biased negatively in roll. The above equation is specifically for a trailing fin in the trailing fins up configuration. Figure 4-5(a) shows the vehicle with its leading fins with a positive roll bias, and trailing fins with a negative roll bias. Figure 4-5(b) shows leading fins with a negative roll bias and trailing fins with a positive roll bias. As in heave motion, the direction of the front fins are reversed,

42

(a) Leading fins up, trailing fins down.   (b) Leading fins down, trailing fins up.
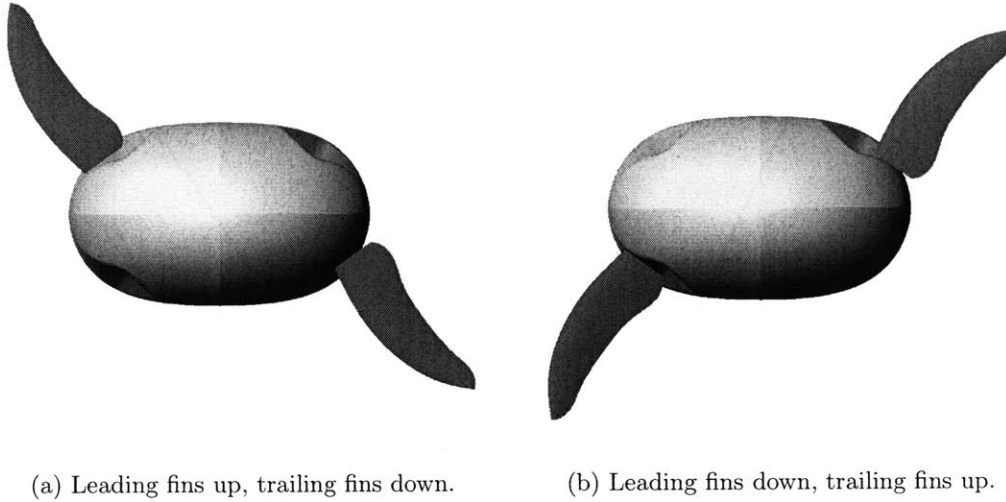
Figure 4-5: Sway fin positions.

minimizing surge motion.

Surge motion, like yaw motion, is also a lift based maneuver. During surge motion, each fin flaps with the twist motion leading the roll motion by 90 degrees. Neither the twist or the roll motion is biased, which creates an average force with only a horizontal component. The equations of motion for an individual fins are

$$\phi(t) = \phi_0 \sin(\omega t) \tag{4.7}$$

$$\theta(t) = \theta_0 \cos(\omega t) \tag{4.8}$$

These equations are identical to the equations of motion for an individual fin in yaw. However, unlike in yaw, all the fins are driven in the same direction.

4.2 Testing Plan

The open loop performance of the BFFAUV was evaluated across four degrees of freedom; surge, sway, heave, and yaw. Within each degree of motion, roll amplitude, twist amplitude, and frequency can be varied to explore a range of possible motions. In some modes of motion, varying certain parameters is more practical than others.

43

Figure 4-6: Fin motion during surge testing.

With heave, the parameters that were varied were roll amplitude ϕ_0 and frequency. ϕ_0 takes on values of 15, 30, and 45 degrees, and frequency is either 0.5 or 1.0 Hz, creating a test matrix with six entries. In sinusoidal drag based forms of motion, using a fi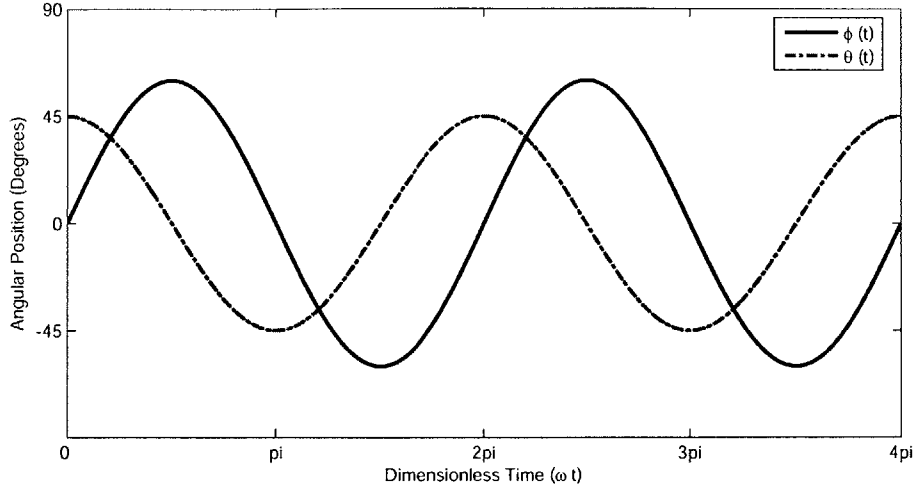xed twist bias of 45 degreed and twist amplitude of 45 degrees creates the rowing motion, so this portion of the motion is not varied. In each heave testing run, the vehicle was started near the surface of the testing pool. The motion of the foils was ramped up from an initial zero position, with the forward foils switched to reversed direction, into the full roll and twist amplitudes. Each test begins with the vehicle descending. The vehicle is commanded to stop its descending foil motion and begin upward heave manually by a user on deck. The end of the run was similarly commanded.

In yaw testing, the parameters that were varied were roll amplitude ϕ_0, twist amplitude θ_0, and frequency. Each parameter was given two values, creating a test matrix with eight entries. phi_0 takes on the values 45 and 60 degrees, θ_0 takes on the values 40 and 60 degrees, and the frequency used is either 0.5 or 1.0 Hz. For yaw testing, a "fast-start" control sequence was used. The foils are positioned to the peak roll angle, equal to the roll amplitude, with the twist amplitude at zero. They

44

then start their full motion from this position, effectively starting in mid-stroke. This motion gives a higher acceleration than a ramped-in "slow-start" sequence. The vehicle itself was manipulated to begin each run at a depth of approximately one meter. The full yaw motion was run 25 seconds. The vehicle was run alternatingly in clockwise and counter-clockwise yaw, to limit tether tangling.

In sway testing, we hold all parameters except frequency fixed. While it's possible to vary the roll amplitude of the strokes, the vehicle's tendency to roll while traveling in sway is exaggerated by having the bias angle further away from 90 degrees. Thus, in sway, the roll bias is held at 54 degrees and the roll amplitude is held at 15 degrees, keeping the peak angle of the motion just under 70 degrees, the maximum angle of roll attainable by the BFFAUV's actuators. Frequency is varied between 1.0 and 1.5 Hz. For each run, the vehicle was positioned below the surface of the pool. In each run, the vehicle was swayed in both "leading fins up, trailing fins down" and "leading fins down, trailing fins up" configurations, as shown in Figures 4-5(a) and 4-5(b). The switch between modes was triggered from on deck.

With surge, as in yaw, roll amplitude and twist amplitude are varied. Frequency is fixed at 1 Hz. Roll amplitude is given three values, 30, 45, and 60 degrees, while twist angle takes on the values of 40 and 60 degrees. This creates a six entry test matrix. For surge tests, the vehicle was fitted with two stabilizer fins at the rear of the vehicle, oriented on the vertical axis. These fins are identical to the actuator foils described in Section 2.1.2. Surge tests were started with the vehicle under the surface. For most of the tests, a fast-start control sequence was used for all of the lower amplitude tests similar to the sequence used for yaw testing. For the most aggressive motion, with roll amplitude of 60 and twist amplitude of 40, a slow-start sequence was used. The actuators were not able to achieve the fast-start motion at these amplitudes.

4.3 Measurement Techniques

Each mode of motion requires a different measurement approach. With a range of sensors including forward- and side-looking altimeters, an inertial measurement unit, and a Doppler Velocity Log, the method of measuring performance can be tailored to each mode of motion.

Heave motion is most easily measured by the downward-looking altimeter. The altimeter is able to deliver position data at a high sample rate. In our experiments, a sample rate of 66.67 Hz was used. The time-scale of the operation of the BFFAUV is slow relative to the sample rate, so the time traces of position from the altimeter are smooth and differentiable after moderate filtering. To smooth the recorded data, a 4th degree Butterworth filter with a cut-off frequency of 0.33 Hz was used. The maximum value of ascent and descent are both considered.

Yaw motion is most accurately measured with the angular rate gyros of the accelerometer. The sample rate used for this measurement is 66.67 Hz. The rate gyros of the accelerometer have an inherent bias. Calibration data is taken while the vehicle is sitting on deck, allowing a steady calibration. Using the calibration, a relatively accurate measurement of the yaw rate can be found. Again, a 4th degree Butterworth filter with a cut-off frequency of 0.33 Hz was used to filter the data. The maximum velocity achieved in this filtered data is considered to be maximum attained velocity.

Sway velocity is most easily measured using the Doppler Velocity Log. The DVL directly measures vehicle velocity, compensating for the tilt of the vehicle. The DVL sample rate is approximately 2.2 Hz. During sway testing, monitoring the roll angle of the vehicle is important. The DVL has a limited range of tilt tolerance due to the orientation of the beams. The DVL velocity readings are relatively accurate while the DVL is tilted in roll up to approximately 25 degrees. This places a limit on the maximum sway velocity that can be accurately tracked. The maximum reliably measured sway velocity found is considered as the vehicle's maximum sway velocity.

There are many possibilities for measuring the vehicle's performance in surge. The DVL provides a simple way to measure the vehicle's velocity in surge. The

vehicle remains relatively level during travel allowing for maximum DVL accuracy. Measuring acceleration during surge is more difficult. Small amounts of vehicle pitch angle can have a significant contribution to the measured acceleration. Measuring the pitch angle of the vehicle becomes an important part of determining the vehicle's surge acceleration. Vehicle pitch can be measured by a few different sensors, including the DVL, but the most accurate measurement of tilt angle is generated from the IMU. Section 4.4 discusses how this adjustment is made.

4.4 Experimental Results

For each mode of motion, at least three measurements were taken for each entry of the test matrix. While there was some variation across each entry of the test matrix, consistent trends are apparent in the data. The results are presented here in the chronological order of the experimental testing.

4.4.1 Heave

Velocity and position data are key results from heave testing. Figure 4-7 shows some typical time series for heave position. In these plots, the typical trajectory of the vehicle during the tests is visible. During each run, the vehicle descended from the surface, starting at an altitude of approximately 3.4 meters from the bottom of the pool, and descended to within one meter altitude of the bottom. Figures 4-8 and 4-9 represent typical time series of velocity data taken from the DVL across the test matrix. A top heave velocity is achieved during both descent and ascent.

The maximum and minimum velocities attained through the range of testing are included Tables 4.1 and 4.2. At the lowest heave rate explored, where flapping frequency is 0.5 Hz and $\phi_0 = 15°$, the vehicle had reduced authority and did not successfully complete all its runs due to the low thrust output of the fins, so measurements taken from those runs represent a rough measurement of the velocity attainable by the vehicle under those parameters of motion. At the other extreme, the highest motion obtained found a peak velocity of 0.5331 m/s. While this number represents the
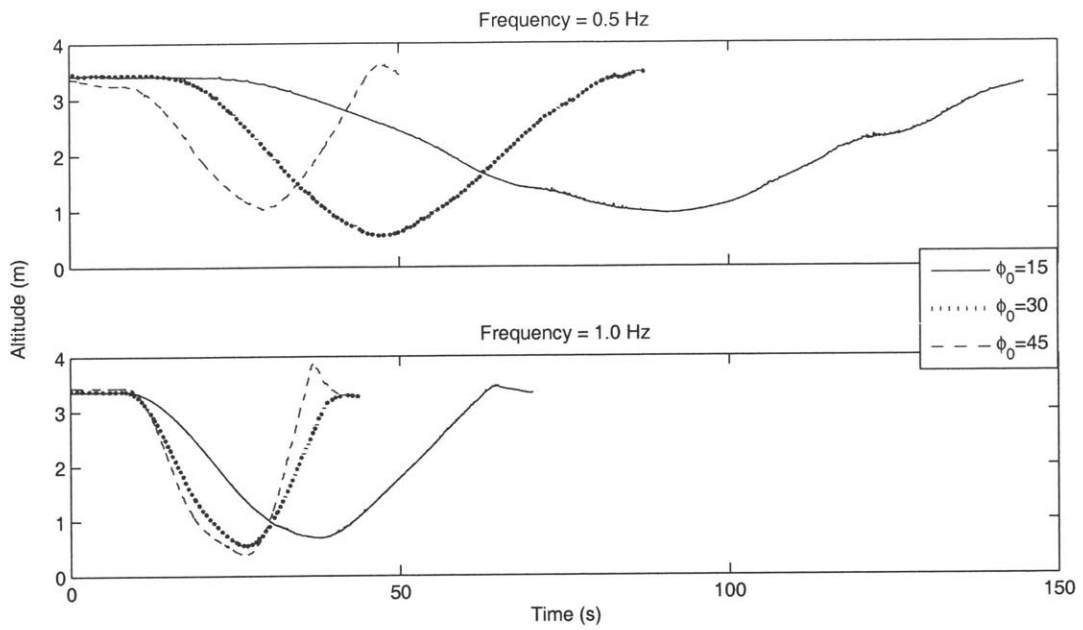
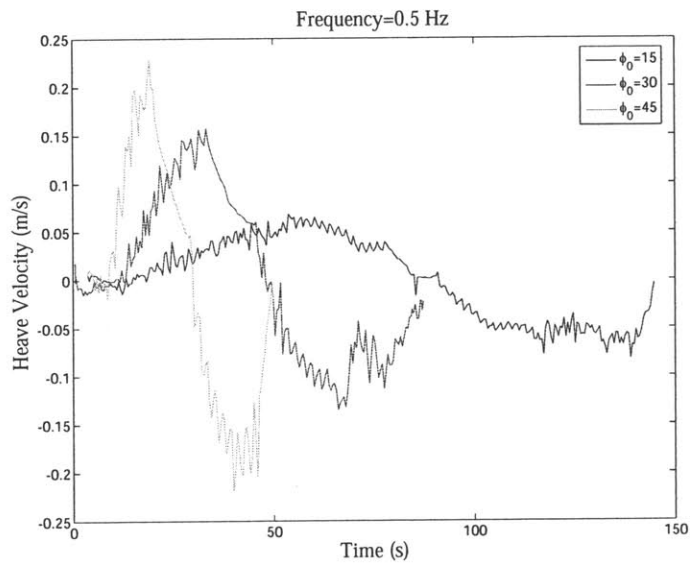47

Figure 4-7: Typical Heave Position Time Series.

Figure 4-8: Typical Heave Velocity Time Series for Frequency=0.5 Hz.
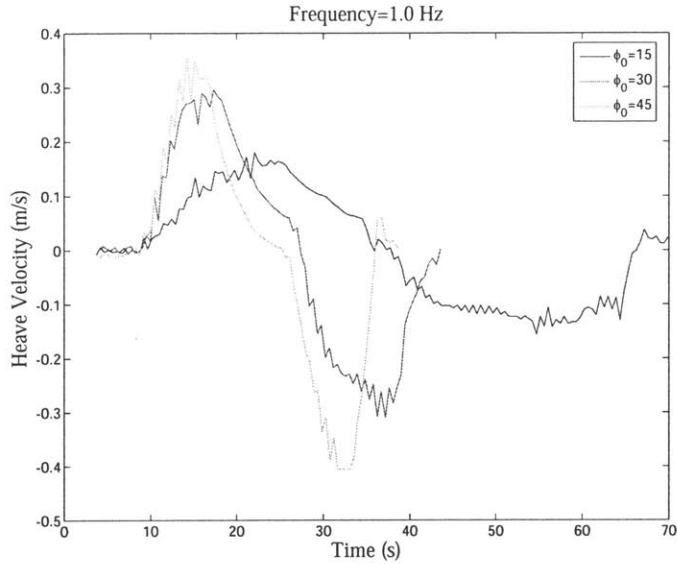
48

Figure 4-9: Typical Heave Velocity Time Series for Frequency=1.0 Hz.

highest velocity found by the DVL, there is clearly a difference between ascending and descending maximum velocities, caused by the buoyancy of the vehicle. The positive buoyancy of the vehicle during these tests biases the velocities such that the ascent velocity is significantly higher. A more accurate estimate of the vehicle's maximum achieved heave velocity can be found by taking the average of all the maximum ascent and descent velocities for a frequency of 1 and a roll amplitude of 45°. This yields a maximum heave velocity of 0.38 meters per second for a well trimmed vehicle.

Table 4.1: Peak Heave Velocities for Frequency=0.5 Hz

ϕ_0	Descent	Ascent
15°	0.0771	0.0864
	0.1041	
30°	0.1485	0.1401
	0.1503	0.1323
45°	0.2244	0.2036
	0.1848	0.2266
	0.2001	0.2193

49

Table 4.2: Peak Heave Velocities for Frequency=1.0 Hz

ϕ_0	Descent	Ascent
15°	0.0679	0.0598
	0.1856	0.1854
	0.1771	0.1637
30°	0.2804	0.3139
	0.2964	0.2863
	0.2892	0.3087
45°	0.3106	0.4338
	0.3306	0.4279
	0.3657	0.5331
	0.3424	0.4203

4.4.2 Yaw

For yaw motion, maximum yaw velocity achieved is the primary measurement of concern. The reported velocity is based on the velocity rate gyro of the IMU. Figure 4-10 shows a typical plot of yaw velocity for a test run with a flapping frequency of 0.5 Hz, a roll amplitude of 60 degrees, and a twist amplitude of 40 degrees. The raw yaw velocity signal, compensated by the gyro calibration coefficient, is shown, along with the smoothed data filtered as described in Section 4.3. The velocity given in Tables 4.3 and 4.4 is the peak velocity as taken from the filtered data. The maximum velocity achieved, for motion with a frequency of 1.0 Hz, a roll amplitude of 60 degrees, and a twist amplitude of 60 degrees, is given as 82.2780 degrees per second. A better guess of the maximum yaw velocity attainable would be an average of the velocities in that entry of the test matrix, yielding a maximum velocity of 80.2 degrees per second. This maximum velocity may be near the limits of the vehicle. The vehicle was unable to achieve the motion of the highest entry of the test matrix, with a frequency of 1.0 Hz, a roll amplitude of 60 degrees, and a twist amplitude of 40 degrees.

4.4.3 Sway

In a typical sway trial, the vehicle could potentially achieve it highest velocity traveling in either direction. For each run, the highest sway velocity recorded by the DVL
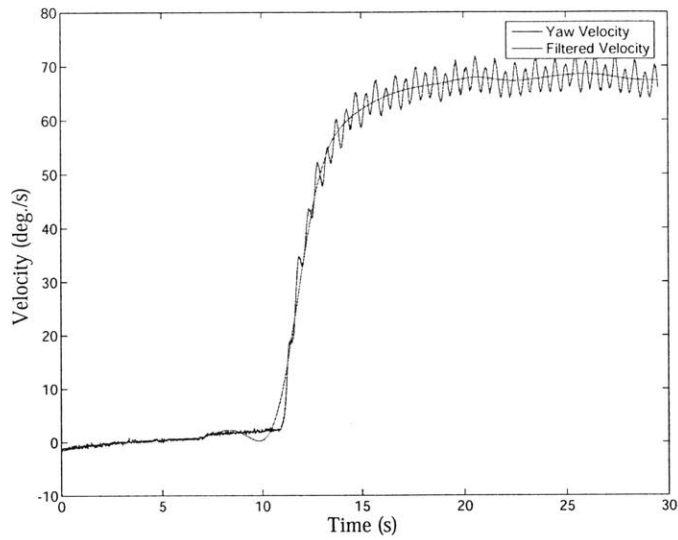
Figure 4-10: A Typical Yaw Angular Velocity Time Series for Frequency=1 Hz, $\phi_0 = 60$, $\theta_0 = 40$.

was reported. Due to space limitations in the testing pool, the vehicle was typically able to travel longer and further on its second leg of travel, and thus typically achieved its maximum velocity during that portion of the testing. This tendency is visible in Figure 4-11, which shows several typical sway profiles.

While the highest sway velocity achieved was 0.4810 meters per second, as shown in Table 4.5, there is some doubt surrounding the ability of the DVL to measure sway velocity under the presence of a high vehicle roll angle. During sway trials with a flapping frequency of 1.5 or 2 Hz, the vehicle roll angle as determined by the IMU rises above the suggested maximum advisable roll angle of approximately 25 degrees. This high roll angle compromises both the pure translational quality of the motion as well as the accuracy of the measurement techniques used to record performance.

Table 4.3: Peak Yaw Velocities for Frequency=0.5 Hz

	$\theta_0 = 60°$	$\theta_0 = 40°$
$\phi_0 = 45°$	34.6354	36.4274
	31.3932	30.8079
	33.5544	31.1204
	29.2052	
$\phi_0 = 60°$	37.3474	41.466
	32.2234	36.7384
	34.5227	

Table 4.4: Peak Yaw Velocities for Frequency=1.0 Hz

	$\theta_0 = 60°$	$\theta_0 = 40°$
$\phi_0 = 45°$	69.457	71.892
	68.4221	71.8299
	71.2739	70.56
	70.3155	72.8048
$\phi_0 = 60°$	79.8225	
	78.7758	
	82.2780	
	79.9362	

4.4.4 Surge

With surge performance, both velocity and acceleration are important results. In a typical surge test run, the vehicle accelerates from a standstill to nearly full velocity over the course of about 5 seconds. Figure 4-12 shows typical surge time series. Table 4.6 shows the peak velocities attained by the vehicle during these surge trials. The peak velocity is the highest velocity reported by the DVL. Figures 4-13-4-18 show the time series for each parameter set individually. The variation in measurements at the higher ranges of motion reflects the limitations of the testing set-up. The length of the pool limits the safe travel distance of the vehicle. Because of the limitations placed on the vehicle due to the pool length and the length of its tether, the vehicle may not always reach its full velocity due to the premature ending of the test runs. Taking the average of the velocities for flapping frequency of 1.5 Hz, roll amplitude
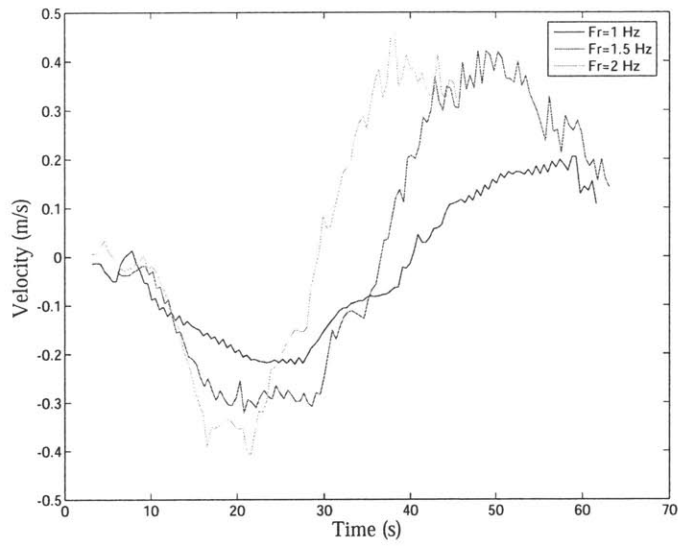
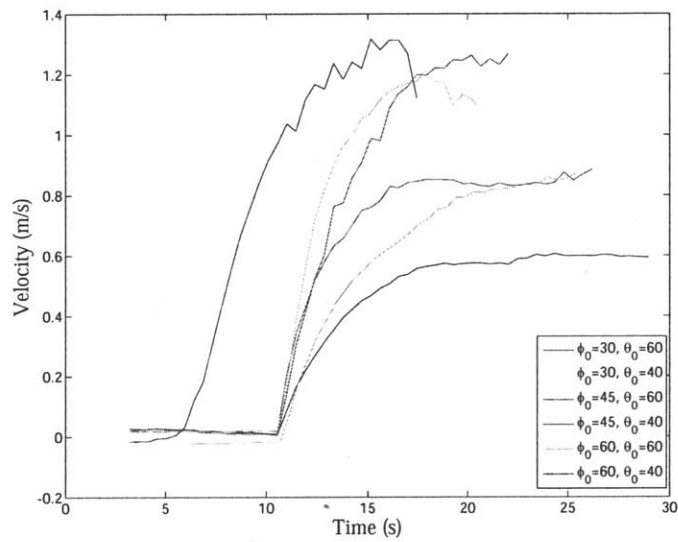Figure 4-11: Typical Sway Velocity Time Series.

Figure 4-12: Representative time series of DVL Surge Velocity for Frequency=1 Hz.

53

Table 4.5: Peak Sway Velocities (m/s)

	$Fr = 1.0$ Hz	$Fr = 1.5$ Hz	$Fr = 2.0$ Hz
$\theta_0 = 15°$	0.2080	0.3130	0.4810
	0.2100	0.3750	0.4083
	0.2210	0.3250	0.4810

of 60 degrees, and twist amplitude of 40 degrees, the peak attained surge velocity is 1.38 meters per second. This velocity may be near the peak attainable velocity for the vehicle in this testing space. The vehicle is unable to achieve the given motion with a "fast-start" control sequence, instead ramping up to this velocity. A higher velocity may be attainable in a larger testing space if the vehicle is able to ramp into higher flapping frequencies.

Table 4.6: Surge velocities for Frequency=1 Hz

	$\theta_0 = 60°$	$\theta_0 = 40°$
$\phi_0 = 30°$	0.638	0.886
	0.606	0.873
	0.606	0.942
		0.889
		0.923
$\phi_0 = 45°$	0.885	1.243
	0.906	1.267
	0.855	1.241
$\phi_0 = 60°$	1.301	1.365
	1.214	1.317
	1.17	1.466

The ability of the vehicle to accelerate is reflected by the period of time required for the vehicle to accelerate to its peak velocity. To estimate the performance of the vehicle in this manner, the time from the start of the motion to 90% of full velocity is recorded in Table 4.7. The final entry of the table is left blank because the "fast-start" control sequence was not used for those tests, thus time to 90% of velocity is much higher than trends in the table would suggest.

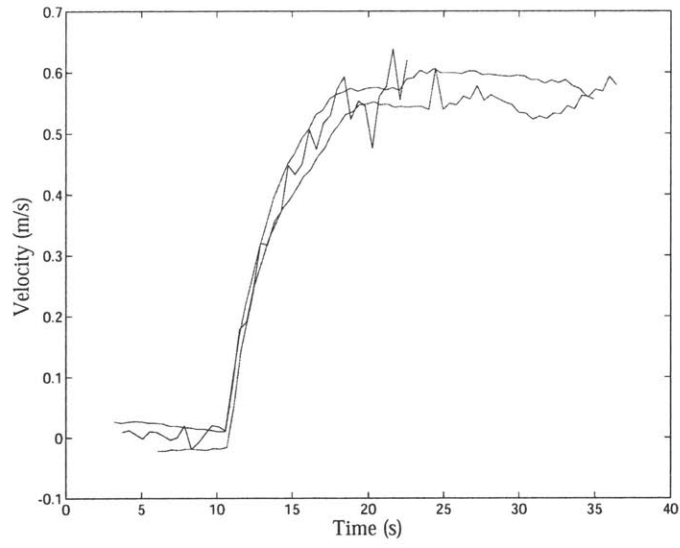Another way to measure the performance of the vehicle in surge acceleration

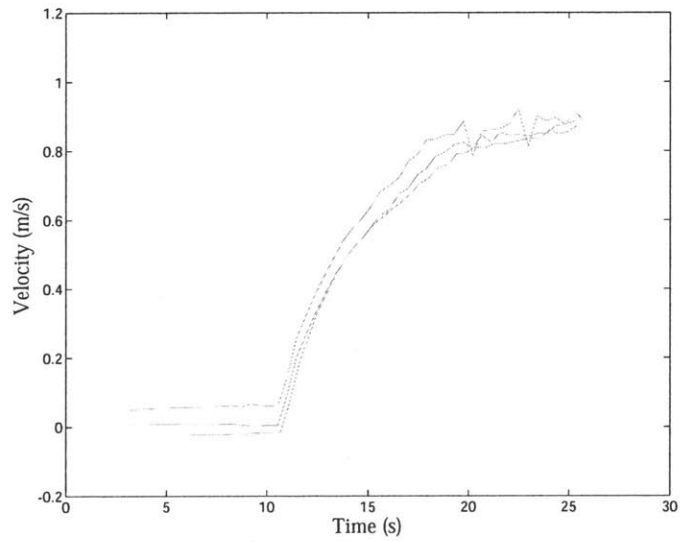Figure 4-13: Surge time series for $\phi_0 = 30$, $\theta_0 = 60$.

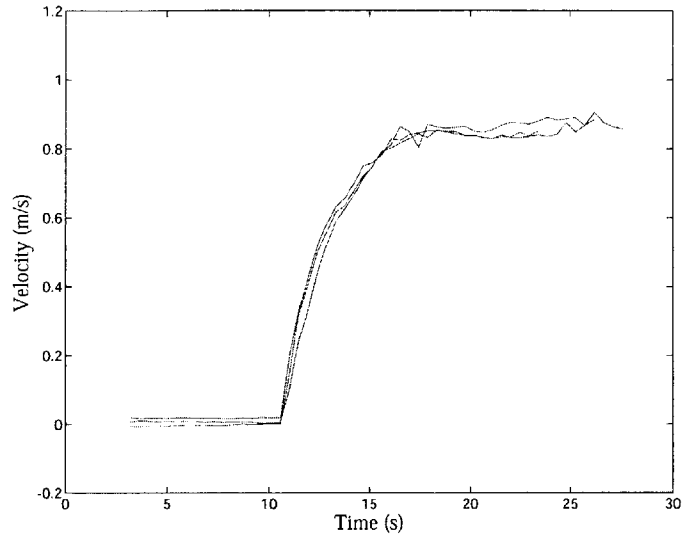Figure 4-14: Surge time series for $\phi_0 = 30$, $\theta_0 = 40$.

55

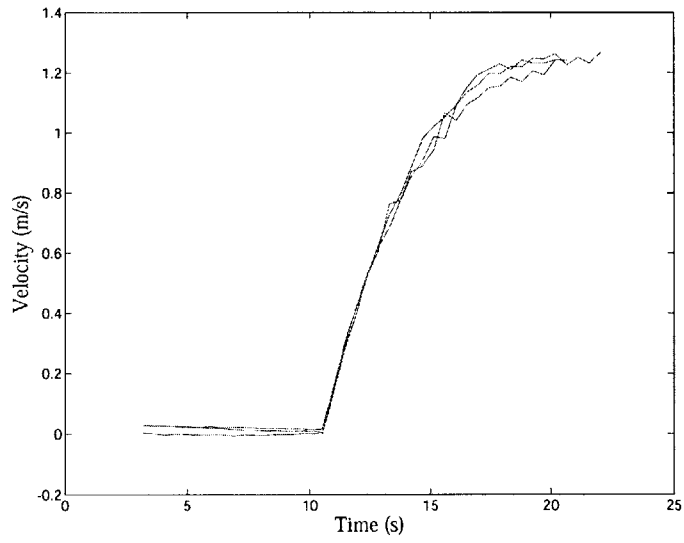Figure 4-15: Surge time series for $\phi_0 = 45$, $\theta_0 = 60$.

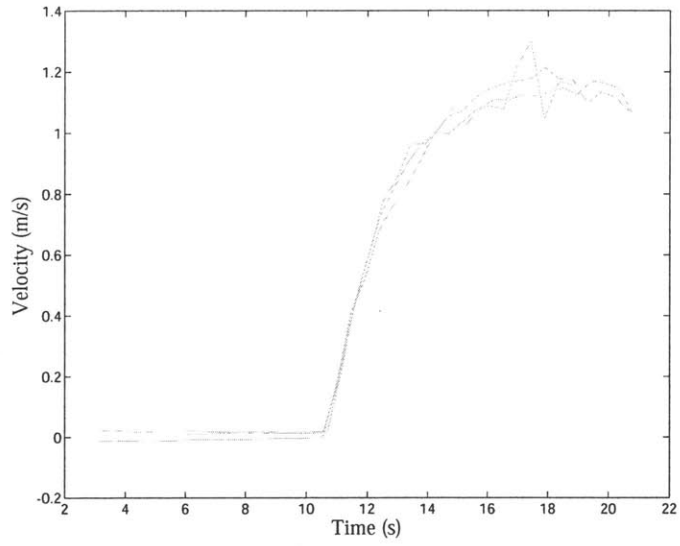Figure 4-16: Surge time series for $\phi_0 = 45$, $\theta_0 = 40$.

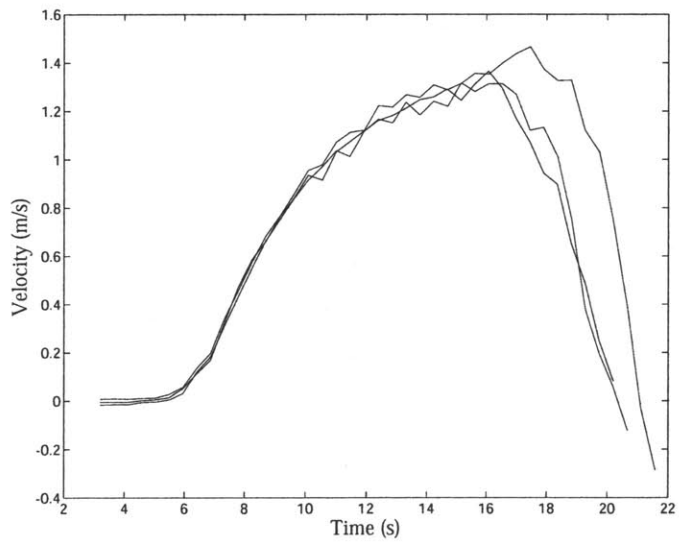Figure 4-17: Surge time series for $\phi_0 = 60$, $\theta_0 = 60$.

Figure 4-18: Surge time series for $\phi_0 = 60$, $\theta_0 = 40$.

57

Table 4.7: Surge 90% Velocity Times (s) for Frequency=1 Hz

	$\theta_0 = 60°$	$\theta_0 = 40°$
$\phi_0 = 30°$	7.4	8.3
	6.9	7.8
	8.3	7.4
$\phi_0 = 45°$	5.0	5.5
	5.5	6.0
	4.6	6.4
$\phi_0 = 60°$	5.5	
	4.6	
	5.5	

is to observe the velocity profiles from DVL. By calculating the slope of the line drawn between two points of a profile, the rough average acceleration can be found. Table 4.8 shows the maximum slope attained during each trial. From the DVL, the

Table 4.8: Peak DVL Surge Acceleration for Frequency=1 Hz

	$\theta_0 = 60°$	$\theta_0 = 40°$
$\phi_0 = 30°$	0.2019	0.2373
	0.1705	0.2413
	0.1983	0.2393
		0.2419
		0.2441
$\phi_0 = 45°$	0.4167	0.3149
	0.3228	0.3486
	0.3972	0.3026
$\phi_0 = 60°$	0.4989	0.3333
	0.4731	0.2742
	0.5089	0.3100

peak average acceleration was approximately 0.49 m/s^2 for a roll amplitude of 60 degrees and a twist amplitude of 60 degrees. A typical DVL acceleration time series for these kinematics is shown in Figure 4-19. The acceleration peaks sharply and drops off quickly as the vehicle reaches speed. Figure 4-20 shows a typical slow-start acceleration time series for fin kinematics with a frequency of 1 Hz, a roll amplitude of 60 degrees, and a twist amplitude of 40 degrees. The peak acceleration is slower as
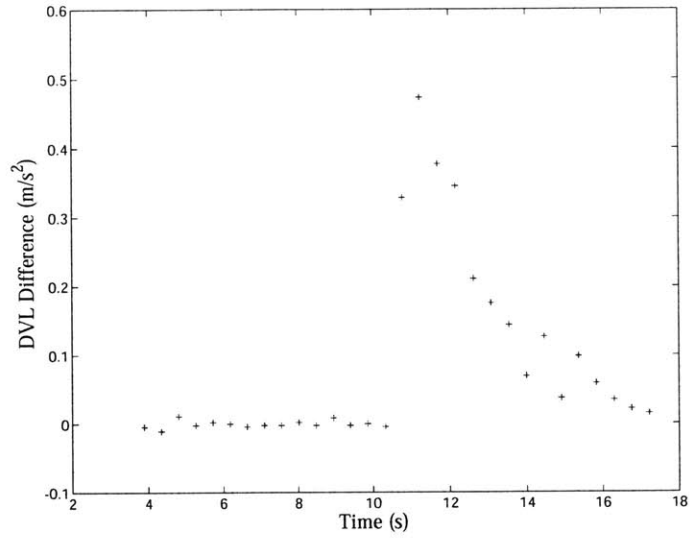
58

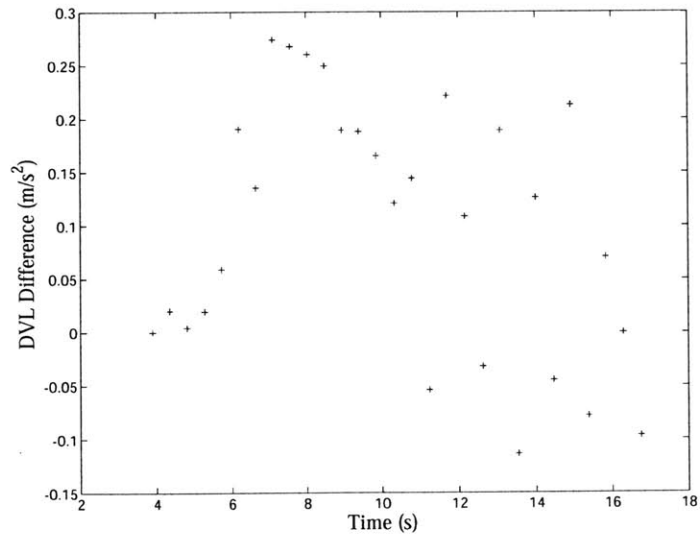Figure 4-19: Typical time series for Fast-Start DVL Acceleration.

Figure 4-20: Typical time series for Slow-Start DVL Acceleration.

59

the fins ramp up to their target amplitudes. Instead of peaking sharply, the higher acceleration is maintained for a few seconds as the vehicle slowly ramps up to its maximum measured velocity.

Trends in the vehicle's surge performance are based on the variation of the roll and twist amplitudes. Higher roll amplitudes correspond to higher maximum velocities and faster accelerations. For example, comparing Figure 4-13, for $\phi_0 = 30$, $\theta_0 = 60$, and 4-17, for $\phi = 60$ and $\theta_0 = 60$, and the corresponding data from Tables 4.6 and 4.8, the maximum velocity reached and the maximum rate of acceleration were both higher for the higher roll amplitude. The effect of twist amplitude on performance is more complicated. A higher twist amplitude leads to a faster acceleration, but a lower twist amplitude corresponds to a higher maximum velocity. For example, for the trial runs with $Fr = 1Hz$, $\phi_0 = 45$, and $\theta_0 = 60$, as shown in Figure 4-15, the average maximum velocity attained was 0.88 meters per second, the average time to 90% of velocity was 5.0 seconds, and the average DVL acceleration was 0.38 meters per second per second. For the corresponding trials with $\theta_0 = 40$, the average maximum velocity attained was 1.25 meters per second, significantly higher than the maximum velocity attained with a higher twist amplitude, but the average time to 90% of velocity was 6.0 seconds and the average DVL acceleration was 0.32 meters per second per second, slower than the the accelerations attained at the higher twist amplitude. With this understanding of the effects of roll and twist amplitudes, the vehicle's performance in surge can be tailored to fit different performance goals. For example, by starting a surge run with a high twist angle and ramping down to lower twist angles, the vehicle could accelerate quickly and still attain high maximum velocities.

Chapter 5

Discussion of Results

The experimental results for the Biomimetic Flapping Foil AUV presented here detail the performance of the vehicle in several modes of motion. The heave, yaw, sway, and surge motion data shown in Chapter 4 sketch out the vehicle's abilities.

The rough maximum cruising velocity of the vehicle was measured to be approximately 1.38 meters per second. This value compares reasonably to projections as discussed in Chapter 3. Licht's [10] prediction of 1.5 to 2 meters per second as the vehicle's maximum velocity may be attainable in a better controlled environment. The limitations of the testing space and the open loop nature of the control sequences may reduce the maximum velocity attained. Results for the lower end of the surge spectrum were also interesting. The predicted value for maximum velocity for flapping frequency of 1 Hz, roll amplitude of 30, and twist amplitude of 40 based on the coefficient of thrust predicted by Lim's [11] data was 1.1 meters per second, but the maximum velocity average across the experimental data was only 0.9026 meters per second. Again, sub-optimal conditions may have contributed to the difference between the predicted and experimental data. Imprecision in the estimates for the vehicle's drag coefficient and other parameters are also likely to have contributed to the difference between the estimated and measured maximum velocities.

Estimates placed the expected angular velocity in yaw at approximately 75 degrees a second, very close to the maximum yaw observed of 80.2 degrees per second. The model used for yaw may place too high a value on the drag coefficient and added mass

of the body, as the estimates for these parameters are based on undisturbed water.

In heave, yaw, and sway, near maximum velocities may have been achieved. In each case, the vehicle was driven until the actuators were unable to attain the desired motion. For heave, the maximum heave velocity measured was 0.3956 meters per second. For yaw, the maximum angular yaw velocity was measured at 80.2 degrees per second. For sway, the maximum sway velocity was measured as 0.4568 meters per second.

5.1 Recommendations for Future Work

Future work with the vehicle could be greatly improved. Improving the test space would be one way to improve vehicle tests in general. The vehicle can travel quickly enough to need a larger space than the available testing pool. In addition to its relatively small size, the pool used for these experiments has currents and jets that can significantly affect the vehicle's performance.

Improved measurement strategies would also improve the quality of the data. The sample rate of the DVL, which is used for many of these measurements, is relatively low, and the DVL can generate unreliable data in high roll and pitch conditions. Sway data are particularly difficult to measure. One possible solution under consideration is using video tracking to measure the vehicle's sway velocity.

Another significant improvement to the vehicle's testing would be closed loop control. Keeping the vehicle on track improves both the quality of the motion and the ability to measure that motion. Adaptive controls may help the vehicle attain its true peak velocities and accelerations.

Bibliography

[1] J. Anderson and N. Chabra. Maneuvering and stability performance of a robotic tuna. *Integrative and Comparative Biology*, 42(1):118–126, February 2002.

[2] David Barrett. The design of a flexible hull undersea vehicle propelled by an oscillating foil. Master's thesis, Massachusetts Institute of Technology, June 1994.

[3] David Beal. *Propulsion Through Wake Synchronization Using a Flapping Foil*. PhD dissertation, Massachusetts Institute of Technology, June 2003.

[4] S. F. Hoerner. *Fluid-Dynamic Drag*. Hoerner Fluid Dynamics, Bakersfield, California, 1965. This is a full BOOK entry.

[5] Michael Jacuba. Design and fabrication of a flexible hull fro a bio-mimetic swimming apparatus. Bachelor's thesis, Massachusetts Institute of Technology, June 2000.

[6] N. Kato and H. Liu. Optimization of motion of a mechanical pectoral fin. *JSME International Journal Series C*, 46(4):1356–1362, December 2003.

[7] N. Kato, H. Liu, and H. Morikawa. Biology-inspired precision maneuvering of underwater vehicles - part 3. *International Journal of Offshore and Polar Engineering*, 15(2):81–87, June 2005.

[8] Naomi Kato. Control performance in the horizontal plane of a fish robot with mechanical pectoral fins. *IEEE Journal of Oceanic Engineering*, 25(1):121–129, January 2000.

[9] John Kumph. The design of a free swimming robot pike. Bachelor's thesis, Massachusetts Institute of Technology, June 1996.

[10] Stephen Licht, Victor Polidoro, Melissa Flores, Franz S. Hover, and Michael S. Triantafyllou. Design and projected performance of a flapping foil auv. *IEEE Journal of Oceanic Engineering*, 29(3), July 2004.

[11] Keith K. L. Lim. Hydrodynamic performance and vortex shedding of a biologically inspired three-dimensional flapping foil. Master's thesis, Massachusetts Institute of Technology, February 2005.

[12] Woei-Min Lin, Gabriel Zee, and Dick K. P. Yue. Development and demonstration of an articulated motion control fin system for a prototype underwater vehicle. Final report, National Defense Center of Excellence for Research in Ocean Sciences (CEROS), June 2005. This is a full TECHREPORT entry.

[13] Craig Martin. Design and performance evaluation of a biomimetic flapping foil. Master's thesis, Massachusetts Institute of Technology, June 2001.

[14] Karl-Magnus Weidmann McLetchie. Force and hydrodynamic efficiency measurements of a three-dimensional flapping foil. Master's thesis, Massachusetts Institute of Technology, May 2004.

[15] M. Nakashima, N. Ohgishi, and K. Ono. A study on the propulsive mechanism of a double jointed fish robot utilizing self-excitation control. *JSME International Journal Series C: Mechanical Systems, Machine Elements, and Manufacturing*, 46(3):982–990, September 2003.

[16] Elizabeth Pennisi. With flippers, two can equal four. *Science*, 307, January 2005.

[17] Jeffrey A. Walker. Does a rigid body limit maneuverability? *Journal of Experimental Biology*, 203:3391–3396, 2000.

[18] P. W. Webb. Kinematics of pectoral fin propulsion in *cymatogaster aggregata*. *Journal of Experimental Biology*, 59:697–710, 1973.

[19] Mark W. Westneat. Functional morphology of aquatic flight in fishes: Kinematics, electromyography, and mechanical modeling of labriform locomotion. *American Zoology*, 36:582–589, December 1996.